Geochemistry Geophysics Geosystems G3

Published by AGU and the Geochemical Society

Article
Volume 11, Number 7
1 July 2010
Q07001, doi:10.1029/2010GC003034
ISSN: 1525-2027

Thermal-mechanical behavior of oceanic transform faults: Implications for the spatial distribution of seismicity

Emily Roland
MIT-WHOI Joint Program in Oceanography, Department of Marine Geology and Geophysics, Woods Hole Oceanographic Institution, 266 Woods Hole Road, Woods Hole, Massachusetts 02540, USA (eroland@mit.edu)

Mark D. Behn
Department of Geology and Geophysics, Woods Hole Oceanographic Institution, 266 Woods Hole Road, Woods Hole, Massachusetts 02543, USA (mbehn@whoi.edu)

Greg Hirth
Department of Geological Sciences, Brown University, 324 Brook Street, Providence, Rhode Island 02912, USA (greg_hirth@brown.edu)

[1] To investigate the spatial distribution of earthquakes along oceanic transform faults, we utilize a 3-D finite element model to calculate the mantle flow field and temperature structure associated with a ridge-transform-ridge system. The model incorporates a viscoplastic rheology to simulate brittle failure in the lithosphere and a non-Newtonian temperature-dependent viscous flow law in the underlying mantle. We consider the effects of three key thermal and rheological feedbacks: (1) frictional weakening due to mantle alteration, (2) shear heating, and (3) hydrothermal circulation in the shallow lithosphere. Of these effects, the thermal structure is most strongly influenced by hydrothermal cooling. We quantify the thermally controlled seismogenic area for a range of fault parameters, including slip rate and fault length, and find that the area between the 350°C and 600°C isotherms (analogous to the zone of seismic slip) is nearly identical to that predicted from a half-space cooling model. However, in contrast to the half-space cooling model, we find that the depth to the 600°C isotherm and the width of the seismogenic zone are nearly constant along the fault, consistent with seismic observations. The calculated temperature structure and zone of permeable fluid flow are also used to approximate the stability field of hydrous phases in the upper mantle. We find that for slow slipping faults, the potential zone of hydrous alteration extends greater than 10 km in depth, suggesting that transform faults serve as a significant pathway for water to enter the oceanic upper mantle.

Components: 8600 words, 10 figures, 1 table.

Keywords: oceanic transform faults; fault rheology; serpentinization; fault mechanics.

Index Terms: 3039 Marine Geology and Geophysics: Oceanic transform and fracture zone processes (1207); 7250 Seismology: Transform faults (1207); 7230 Seismology: Seismicity and tectonics (1207).

Received 7 January 2010; **Revised** 30 March 2010; **Accepted** 1 April 2010; **Published** 1 July 2010.

Roland, E., M. D. Behn, and G. Hirth (2010), Thermal-mechanical behavior of oceanic transform faults: Implications for the spatial distribution of seismicity, *Geochem. Geophys. Geosyst.*, *11*, Q07001, doi:10.1029/2010GC003034.

1. Introduction

[2] The relatively simple fault geometry and well-characterized slip rates associated with oceanic transform faults make them excellent locations for studying earthquake behavior. Several aspects of the mechanical behavior of transform faults are relatively well understood. Total seismic moment release rates and the size of the largest earthquakes are linked to variations in fault properties, such as slip rate and fault length [*Engeln et al.*, 1986; *Bird et al.*, 2002; *Boettcher and Jordan*, 2004]. Furthermore, global observations indicate that oceanic transforms sustain a higher degree of aseismic slip and a relatively narrow seismic fault width compared to continental strike-slip systems [*Bird et al.*, 2002; *Boettcher and Jordan*, 2004]. Geodynamic modeling of normal fault rotations adjacent to transforms [*Phipps Morgan and Parmentier*, 1984; *Behn et al.*, 2002] also demonstrate that oceanic transform faults are mechanically weak. Observations of oceanic earthquakes [*Wiens and Stein*, 1983; *Engeln et al.*, 1986; *Bergman and Solomon*, 1988; *Abercrombie and Ekstrom*, 2001; *Braunmiller and Nábělek*, 2008] indicate that in the oceanic lithosphere, the maximum depth of seismicity is thermally controlled. Therefore, characterizing the temperature structure of oceanic transforms is fundamental for understanding the partitioning of seismic and aseismic slip and for determining the spatial distribution of earthquakes.

[3] Transform fault thermal structure is commonly estimated using analytic solutions that average the temperature predicted from a half-space cooling model across the two sides of the fault [e.g., *McKenzie*, 1969]. Results from these calculations have been used to investigate the temperature control on the depth of earthquakes [*Engeln et al.*, 1986; *Bergman and Solomon*, 1988; *Abercrombie and Ekstrom*, 2001; *Braunmiller and Nábělek*, 2008], and to estimate seismic coupling along oceanic transform faults [*Bird et al.*, 2002; *Boettcher and Jordan*, 2004]. These studies indicate that seismicity is limited to temperatures less than 600°C, consistent with laboratory experiments on olivine [*Boettcher et al.*, 2007]. An alternative method for calculating transform fault thermal structure utilizes geodynamic models that incorporate advective heat transport due to mantle flow [*Phipps Morgan and Forsyth*, 1988; *Shen and Forsyth*, 1992; *Furlong et al.*, 2001]. As discussed by *Behn et al.* [2007] these geodynamic models predict much colder transform thermal structure unless the weakness of the brittle portion of the fault is explicitly included. *Behn et al.* [2007] showed that by incorporating a viscoplastic rheology, the depth to the 600°C isotherm at the fault center is similar to that calculated from the half-space model. However, while this model improved upon previous models, it neglected several key processes such as non-Newtonian viscous flow, hydrothermal circulation, and shear heating, and did not explore the effects of fault length and slip rate.

[4] The primary motivation of our study is to explore the links between hydrothermal circulation, thermal structure, and rheology along oceanic transform faults. Enhanced permeability associated with fracturing provides a mechanism for increased fluid circulation and subsequent alteration of the crust and mantle. Hydrothermal cooling has been shown to significantly influence the thermal structure along highly tectonized parts of the oceanic lithosphere [*Sleep*, 1975; *Phipps Morgan et al.*, 1987; *Phipps Morgan and Chen*, 1993; *Cherkaoui et al.*, 2003]. Metamorphic alteration also occurs when water comes into contact with rocks of mantle composition, evidenced by reduced seismic velocities observed along transform faults [*Detrick et al.*, 1987, 1993; *Van Avendonk et al.*, 1998; *Canales et al.*, 2000] and the presence of altered mantle phases recovered by seafloor dredging [*Dick*, 1989; *Cannat et al.*, 1995]. There are several ways that mantle alteration at transform faults may influence tectonic and petrologic processes. Hydrous mantle minerals are weaker than most other minerals in the oceanic crust and upper mantle [*O'Hanley*, 1996; *Moore et al.*, 1997]. Their presence in fracture zones influences frictional behavior and may control the transition between stable sliding and stick-slip behavior. Although serpentine demonstrates stable sliding at low temperatures, under warmer conditions (>~350°C) a transition to velocity weakening is observed [*Moore et al.*, 1997]. This change in the frictional behavior of serpentine may control the upper depth limit of the seismogenic zone. Additionally, because altered peridotite can contain large amounts of water, hydrated mantle minerals formed along transform faults would also contribute significantly to the water budget of the mantle [*Hacker*, 2008]. For example, serpentine contains up to 14 wt % water in its crystal structure [*O'Hanley*, 1996]. Altered mantle rocks formed in transform fault settings will be advected off axis with plate motion and eventually subducted at convergent margins. In this way, mineralogically bound water along transform faults can influence arc volcanism when dehydration occurs during heating of the subducted slab [*Grove et al.*, 2006].

Table 1. Imposed Boundary Conditions and Material Properties

Symbol	Parameter	Value
ρ	average lithospheric density	3300 kg m^{-3}
ρ_w	water density	1000 kg m^{-3}
η	viscosity	η_0 = 1e19, η_{max} = 1e24 Pa s
k	thermal conductivity	k_0 = 3 W m^{-1} K^{-1}
C_p	specific heat	1000 J Kg^{-1}K^{-1}
Q_{sh}	heat source	2 η_{eff} $\dot{\epsilon}_{II}{}^2$ (shear heating)
L_T	transform fault length	50–500 km
u_0	imposed full slip rate	3–12 cm yr^{-1}
T_s	surface temperature	0°C
T_m	mantle temperature	1300°C
R	gas constant	8.3145 J mol^{-1}K^{-1}
A	preexponential factor	1.1 × 10^5 [*Hirth and Kohlstedt*, 2003]
n	stress exponent	3.5 [*Hirth and Kohlstedt*, 2003]
E	activation energy	520 kJ mol^{-1} [*Hirth and Kohlstedt*, 2003]
μ	coefficient of friction (serpentine)	0.85 (0.1)
C	cohesion	20 MPa
g	gravitational acceleration	9.8 m s^{-1}
Nu	Nusselt number	1–8
C_S	k_{eff} smoothing constant, stress	100
C_D	k_{eff} smoothing constant, depth	4

[5] Here, we develop a more realistic model for oceanic transform fault thermal structure by exploring three important thermal and rheological feedbacks: (1) frictional weakening due to mantle alteration, (2) shear heating, and (3) enhanced hydrothermal cooling associated with brittle deformation. We incorporate these feedbacks into numerical models that simulate mantle flow using a viscoplastic rheology, similar to the *Behn et al.* [2007] model, but with the temperature-dependent viscous flow law replaced with a nonlinear power law appropriate for non-Newtonian dislocation creep. We discuss our predicted thermal structure for a range of fault lengths and slip rates. Our findings are then related to the observed distribution of seismicity in a number of settings and the extent of alteration of the oceanic upper mantle.

2. Methods

2.1. Model Setup

[6] We use the finite element software package, COMSOL Multiphysics v.3.5, to solve for conservation of mass, momentum and energy assuming steady state incompressible flow:

$$\nabla \cdot \mathbf{u} = 0 \tag{1}$$

$$\rho(\mathbf{u} \cdot \nabla)\mathbf{u} = \nabla \cdot \left[-pI + \eta\left(\nabla\mathbf{u} + (\nabla\mathbf{u})^T\right)\right] \tag{2}$$

$$\nabla \cdot (-k\nabla T) = Q_{sh} - \rho C_p(\mathbf{u} \cdot \nabla)T. \tag{3}$$

In the conservation equations outlined above, **u** is velocity, T is temperature and p is pressure. Other symbols represent constants and material properties, which are described in Table 1. We assume the infinite Prandtl number approximation, for which the left-hand side of equation (2) is negligible. COMSOL has been benchmarked for non-Newtonian temperature-dependent flow in geologic settings [*van Keken et al.*, 2008], and used previously to model mantle flow and temperature structure around oceanic transform faults [*Behn et al.*, 2007].

[7] We model a ridge-transform-ridge system in which a transform fault of length, L_T, offsets two ridge segments, each extending a distance, L_T/2, on either side of the transform (Figure 1). In this way, the lateral extent of the model domain is dependent on the fault length, with dimensions of $2L_T$ in the along-fault (X) direction, and L_T in the fault-perpendicular (Y) direction (Figure 1). All models extend to a depth of 100 km. The model domain was chosen such that the sides and bottom of the model do not influence the solution. Mantle flow is driven by imposing a surface velocity with a half slip rate, u_0/2, on either side of the fault. The boundary conditions on the sides and bottom of the model are stress-free, allowing convective flux in and out of the model space and mantle upwelling from below. Temperature is fixed to T_s = 0°C and T_m = 1300°C at the surface and bottom boundaries of the model space, respectively (Figure 1).

[8] Numerical solutions for the temperature and flow field are determined using a 3-D mesh of second-order brick elements with finer grid spacing

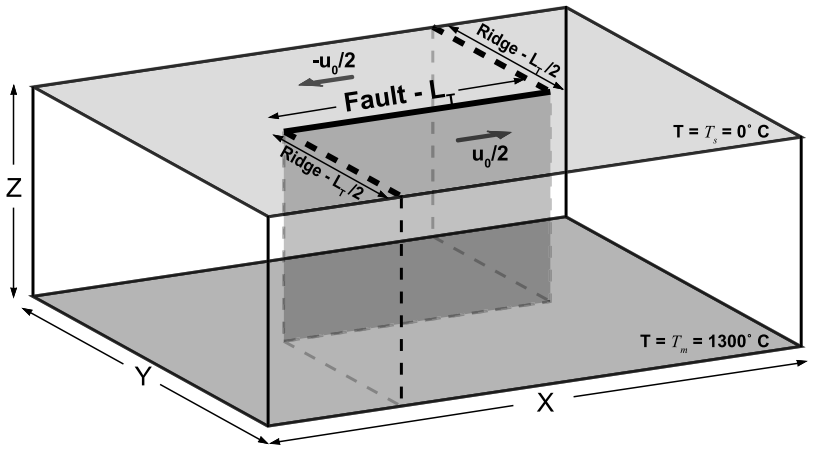

Figure 1. Model geometry. A transform fault of length L_T offsets two ridge segments of length $L_T/2$. The 3-D steady state incompressible mantle flow is driven by an imposed full slip rate, u_0, at the surface. Sides and bottom of the model space are stress-free. The top and bottom of the model are set to 0°C and 1300°C, respectively.

at shallow depths and along the fault plane. We tested a range of gridded mesh spacings along the fault-parallel and fault-perpendicular directions, to insure that the grid spacing is sufficiently fine as to not influence the model solutions. Exact numerical grid spacing of the models presented here varies for different fault length solutions to minimize computation time while still maintaining the insensitivity to mesh spacing. For a 100 km fault model, we use an ~8 km mesh along the x direction and a ~7 km mesh along the y direction. The numerical solution follows a basic Newton method of residual minimization, with a convergence criterion based on a weighted Euclidean norm and a tolerance of 1e-6 for the estimated relative error. Full slip rates modeled here range from 3 to 12 cm/year, and we explore solutions for transform faults with lengths ranging from L_T = 50–500 km.

2.2. Rheology Model

[9] We develop a rheologic model for oceanic transform faults using deformation laws that simulate the processes we expect to occur in transform settings. In the oceanic lithosphere, permanent deformation is accommodated by two primary mechanisms. At shallow depths, yielding occurs by brittle failure along preexisting fault planes and can be described by a linear, pressure-dependent friction law. Deeper in the lithosphere, viscous flow dominates deformation, characterized by thermally activated dislocation creep. To account for both of these processes, we employ a nonlinear viscous rheology with a plastic approximation that allows for brittle weakening in the shallow, cooler part of the lithosphere.

[10] Where temperatures are sufficiently high for rocks to deform by dislocation creep, strain rate and differential stress are related through a temperature-dependent non-Newtonian power law rheology [*Kirby*, 1983]:

$$\dot{\epsilon}_a = A(\sigma_1 - \sigma_3)^n \exp\left(-\frac{E}{RT}\right). \tag{4}$$

The parameters in equation (4) are determined from triaxial experiments, where $\dot{\epsilon}_a$ represents the axial strain rate, $\sigma_1 - \sigma_3$ is the differential stress, and R is the gas constant. We use values for A, the pre-exponential constant, n, the power law exponent, and E, the activation energy appropriate for dry olivine [*Hirth and Kohlstedt*, 2003] (Table 1).

[11] To incorporate the experimentally derived flow law into our viscoplastic rheology model, we calculate a "creep viscosity" (η_{creep}) that is a function of the strain rate and temperature everywhere within the model. The expression for η_{creep} is derived from equation (4) and the isotropic stress-strain relation, $\sigma_{ij} = 2\eta\dot{\epsilon}_{ij}$ such that:

$$\eta_{creep} = \frac{1}{4}\left(\frac{4}{3A}\right)^{\frac{1}{n}}\left(\frac{\dot{\epsilon}_{II}}{\sqrt{2}}\right)^{\frac{1-n}{n}}\exp\left(\frac{E}{nRT}\right). \tag{5}$$

This relation follows from the assumption that, for an incompressible material, the axial strain rate ($\dot{\epsilon}_a$) in equation (4) can be related to the second invariant of the strain rate tensor, $\dot{\epsilon}_{II}$ [*Chen and Morgan*, 1990].

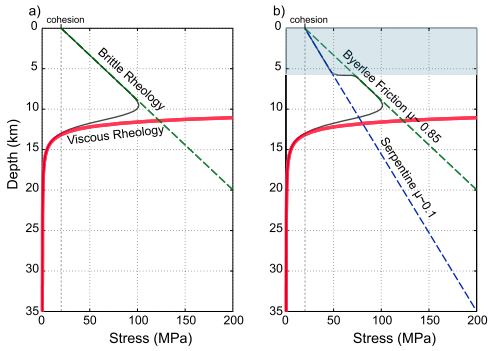

Figure 2. Differential stress versus depth at the center of the transform for the viscoplastic composite rheology (black solid lines). (a) The brittle mechanism described by Byerlee's Law (green dashed line) is dominant at shallow depths and the nonlinear viscous dislocation creep law (red line) dictates deformation at depth. (b) Similar to Figure 2a but with the friction law adjusted with a lower friction coefficient (blue dashed line) in the region where metamorphic alteration is predicted (shaded) simulating weaker serpentinized rocks.

[12] In the cooler lithosphere, where deformation occurs by brittle failure, we use the Coulomb friction criteria to calculate the maximum stress. The maximum shear stress, $\tau_{\max}$, is a function of the friction coefficient, μ, the cohesive strength, C, and the effective normal stress, $\bar{\sigma}_n$, acting on the fault plane:

$$\tau_{\max} = \mu\bar{\sigma}_n + C. \tag{6}$$

The shear and effective normal stresses can be represented in terms of the maximum and minimum principal effective compressive stresses, $\bar{\sigma}_1$ and $\bar{\sigma}_3$ [*Zoback and Townend*, 2001]:

$$\bar{\sigma}_1 = f_1(\mu)\,\bar{\sigma}_3 + f_2(\mu, C), \tag{7}$$

where

$$f_1(\mu) = \frac{\sqrt{\mu^2+1}+\mu}{\sqrt{\mu^2+1}-\mu}, \quad \text{and} \quad f_2(\mu, C) = \frac{2C}{\sqrt{\mu^2+1}-\mu}. \tag{8}$$

For a mid-ocean ridge setting, we assume that $\bar{\sigma}_1$ is the effective vertical stress, $\bar{\sigma}_v = (\rho - \rho_w)gh$. The maximum differential stress supported within the lithosphere, $\Delta\sigma_{brittle}$, can then be expressed in terms of the effective vertical stress, the coefficient of friction and the cohesion:

$$\Delta\sigma_{brittle} = \bar{\sigma}_v\frac{f_1(\mu)-1}{f_1(\mu)} + \frac{f_2(\mu, C)}{f_1(\mu)}. \tag{9}$$

[13] We incorporate the brittle deformation law into our rheology model by specifying a "frictional viscosity" (η_{fric}) that is a function of the maximum stress calculated from our brittle law (equation (9)) and the strain rate [*Chen and Morgan*, 1990]:

$$\eta_{fric} = \frac{\Delta\sigma_{brittle}}{2\sqrt{2}\dot{\epsilon}_{II}}. \tag{10}$$

η_{fric} forces the flow in our model to be consistent with the maximum stress in regions where the brittle failure criteria controls deformation. We use η_{fric} in our composite rheology to mimic properties of a plastic rheology within the context of a viscous model.

[14] The assumption that $\bar{\sigma}_1 = \bar{\sigma}_v$ made in the above formulation is valid for tectonic settings under horizontal extension, and is therefore appropriate for most of the mid-ocean spreading ridge environment. For simplicity, we assume this is valid everywhere within the model space, acknowledging that $\bar{\sigma}_v = \bar{\sigma}_2$ within the transform domain. Applying this assumption within the transform allows strike-slip fracture planes to fail at a slightly lower differential stress than theoretically predicted. However, as we show in section 3.1, decreasing the coefficient of friction has a relatively small effect on the predicted flow field and derived temperature structure, and thus should not greatly influence our model results.

[15] To incorporate both brittle and viscous deformation mechanisms into a composite rheological model, we assume that under a given set of conditions, deformation occurs by the mechanism with the smallest viscosity. This is accomplished by calculating an effective viscosity such that:

$$\eta_{eff} = \left(\frac{1}{\eta_{creep}} + \frac{1}{\eta_{fric}} + \frac{1}{\eta_{\max}}\right)^{-1}. \tag{11}$$

η_{eff} is specified in equation (2) to compute the flow field. The third term in equation (11) represents a maximum viscosity that is included to aid numerical convergence. In our solution process, mantle flow and temperature are first calculated for a constant viscosity ($\eta_0 = 10^{19}$ Pa s). We use the strain rate from the initial solution to calculate viscosity values (equations (5) and (10)) and incorporate the composite rheology (equation (11)) in the flow laws of subsequent solutions. We then iteratively increase the maximum viscosity term in our composite rheology, from $\eta_{\max} = \eta_0$ to 10^{24} Pa s. A stress versus depth profile beneath the transform that results from this composite rheology model is displayed in Figure 2a.

[16] The constitutive equations and rheology model outlined thus far compose our base model. We build upon this base model by exploring three additional rheological and thermal feedbacks that simulate processes that potentially influence fault temperature and stress conditions.

2.3. Frictional Weakening

[17] In a transform environment, the lithosphere deforms brittlely to depths that extend into the upper mantle [*Brace and Kohlstedt*, 1980; *Kirby*, 1983]. Increased permeability associated with brittle cracking may provide a conduit for seawater to come into contact with mantle rocks, leading to alteration. The presence of hydrated phases in the oceanic lithosphere has important implications for the mode of brittle failure. Laboratory studies demonstrate that rocks with even a small degree of serpentinization may be significantly weaker than unaltered peridotite [*Escartin et al.*, 2001].

[18] We incorporate the effects of mechanical weakening associated with serpentinization by modifying equation (9) when two conditions are met: (1) deformation occurs brittlely ($\eta_{fric} < \eta_{creep}$) and (2) serpentine or talc is stable based on the stability fields of *Poli and Schmidt* [2002] for water-saturated peridotites. For a hydrous lherzolite composition, serpentine is stable at temperatures below 540°C and talc is stable for temperatures between approximately 540°C–640°C at a depth of 10 km (pressures of ~ 300 MPa) [*Poli and Schmidt*, 2002]. In serpentinized regions, the coefficient of friction (μ) in equations (6)–(9) is adjusted from the unaltered olivine value of 0.85 to 0.1, the lower lab-derived value appropriate for lizardite, chrysotile, and talc [*Reinen et al.*, 1994; *Moore et al.*, 1997]. A schematic diagram showing a stress profile that reflects our composite viscoplastic rheology modified by the effects of serpentinization is shown in Figure 2b.

2.4. Shear Heating

[19] During deformation, most dissipated mechanical energy is converted into heat, increasing the temperature in zones of localized strain. Analytical calculations demonstrate that shear heating will result in considerable heat production along faults that support shear stresses ≥10 MPa [*Fleitout and Froidevaux*, 1980]. To analyze the importance of shear heating in transform settings, we incorporate a heat source term into equation (3) that represents the rate of energy dissipation per unit volume due to viscous dissipation. This value is the product of the stress and strain rate. Using the isotropic stress-strain equation [*Chen and Morgan*, 1990, section 2.2], we calculate the heat source term as a function of the strain rate invariant and the viscosity [*Brun and Cobbold*, 1980]:

$$Q_{sh} = 2\,\eta_{eff}\,\dot{\epsilon}_{II}^{2}, \tag{12}$$

where η_{eff} is taken from equation (11).

2.5. Hydrothermal Cooling

[20] In young oceanic crust, heat flow patterns are strongly affected by convection of seawater through regions of the lithosphere that experience brittle cracking and enhanced permeability [*Phipps Morgan and Chen*, 1993]. We approximate the effects of hydrothermal cooling by increasing thermal conductivity [e.g., *Sleep*, 1975; *Phipps Morgan et al.*, 1987; *Cherkaoui et al.*, 2003] in regions of predicted brittle failure and fluid circulation. In our model, this increase in conductivity is simulated by a Nusselt number (Nu), which represents the ratio of the total heat transport within a permeable layer to heat transfer by conduction alone [*Phipps Morgan et al.*, 1987]. We investigate results for Nu = 1–8 to simulate different efficiencies of hydrothermal cooling. The upper end of this range is motivated by *Phipps Morgan and Chen* [1993], who found that Nu = 8 was required to match seismic velocity observations of the presence and depth of a steady state magma lens over a range of spreading rates.

[21] Temperatures recorded in hydrothermal vent discharge [*Phipps Morgan et al.*, 1987] and geochemical data [*Bonatti and Honnorez*, 1976; *Francis*, 1981; *Kelley and Gillis*, 2002] indicate that hydrothermal circulation may extend to lithospheric depths corresponding to temperatures of 400°C to 700°C. These data suggest that the depth limit of hydrothermal fluid circulation is controlled by the maximum depth of brittle failure. Here, we constrain the region of simulated hydrothermal cooling to be within the predicted zone of brittle failure (i.e., the zone in which our brittle rheology law dominates the effective viscosity). To simulate a decrease in permeability with depth, we decrease the efficiency of hydrothermal cooling, down to a reference depth (z_{ref}), below which we assume fractures are closed by the overburden pressure [e.g., *David et al.*, 1994; *Cherkaoui et al.*, 2003].

[22] This hydrothermal feedback is incorporated into equation (3) via an effective thermal conductiv-

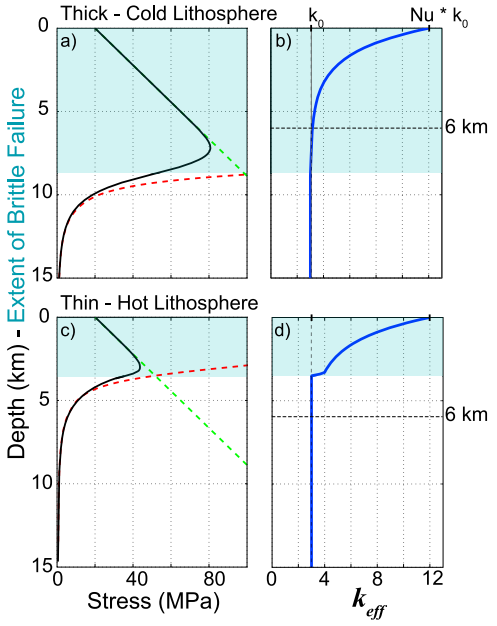

Figure 3. Effective thermal conductivity versus depth, used to simulate hydrothermal cooling for two end-member thermal/stress regimes. The shaded region indicates the extent of brittle deformation. (a and b) In regions where the lithosphere is cool and thick, permeability decreases exponentially with depth down to Z_{ref} = 6 km, as illustrated by the blue line in Figure 3b. (c and d) In regions where the lithosphere is hot and weak, hydrothermal circulation is confined to the brittlely deforming zone. Under these conditions, increased values of thermal conductivity are reduced to the reference value smoothly across the brittle-ductile transition via an error function, as indicated by the blue line in Figure 3d.

ity, k_{eff}, that is a function of Nu, z_{ref} and the ratio of the differential stress associated with the brittle and viscous deformation laws:

$$k_{eff} = k_0\left\{1 + (Nu - 1) \times 0.5\left[1 - erf\left(C_S \log\left(\frac{\Delta\sigma_{brittle}}{\Delta\sigma_{creep}}\right)\right)\right] \times \exp\left(C_D \frac{z}{z_{ref}}\right)\right\}, \quad (13)$$

where k_0 represents the reference thermal conductivity without hydrothermal circulation (Table 1). The error function and exponential terms in this expression, with the associated nondimensional constants C_S and C_D, control the smoothness of the effective conductivity across the brittle-ductile transition and with depth, respectively. In warm/thin lithosphere, where only a thin region deforms brittlely, hydrothermal circulation is limited to the shallow brittle zone, decreasing to the reference conductivity value at the maximum depth of brittle failure (Figures 3c and 3d). In cold/thick lithosphere, brittle deformation likely extends to depths at which the overburden is too high for connected cracks to be supported. Under these conditions, the maximum depth of the hydrothermal cooling is controlled by the effect of overburden pressure on permeability (Figures 3a and 3b).

3. Model Results

[23] The thermal structure calculated using our base model is displayed in Figure 4 for a full slip rate (u_0) of 3.0 cm/yr and transform length (L_T) of 100 km. One key feature of these results is the mantle upwelling in the center of the transform beneath the zone of high strain rate and lower effective viscosity. In this zone, advection of hot mantle leads to warmer temperatures relative to the surrounding lithosphere of the same age (Figures 4a and 4d). The combined effects of conductive cooling with distance from the ridge and advective heating in the center of the fault result in a relatively uniform thermal structure along the fault, with no significant shoaling of the isotherms except near the fault ends (Figures 4b and 4c). These general characteristics of the thermal structure are consistent over the full suite of model parameters we examined.

[24] To compare differences in individual model runs, we characterize solutions in terms of the maximum depth of the 600°C isotherm (Z^m_{600}) and the area above the 600°C isotherm (A_{600}). We also calculate the area between the 350°C and 600°C isotherms ($A_{350–600}$). As discussed above, the 350°C and 600°C isotherms likely represent the lower and upper temperature bounds on the seismogenic zone in mantle rocks. Using these parameters, we can quantify the dependence of the temperature structure on slip rate and fault length. As slip rate decreases from 12 to 3 cm/yr, Z^m_{600} deepens from approximately 4.0 to 7.3 km in models with L_T = 100 km (Figure 5b). Similarly, both A_{600} and $A_{350–600}$ increase with decreasing slip rate (Figure 5a). The area of the seismogenic zone also correlates with fault length (Figure 6). For longer faults, A_{600} increases due to the greater contribution of conductive cooling near the center of the fault. For example, for a slow slipping fault (u_0 = 3 cm/yr), A_{600} increases by approximately an order of magnitude between solutions with L_T = 50 and 200 km. This change is also observed in Z^m_{600}, which deepens from ~5 to 10 km between L_T = 50 and 200 km.

[25] When we compare our model results to a half-space cooling model, we find that estimates of A_{600} and $A_{350–600}$ are remarkably similar for a range of

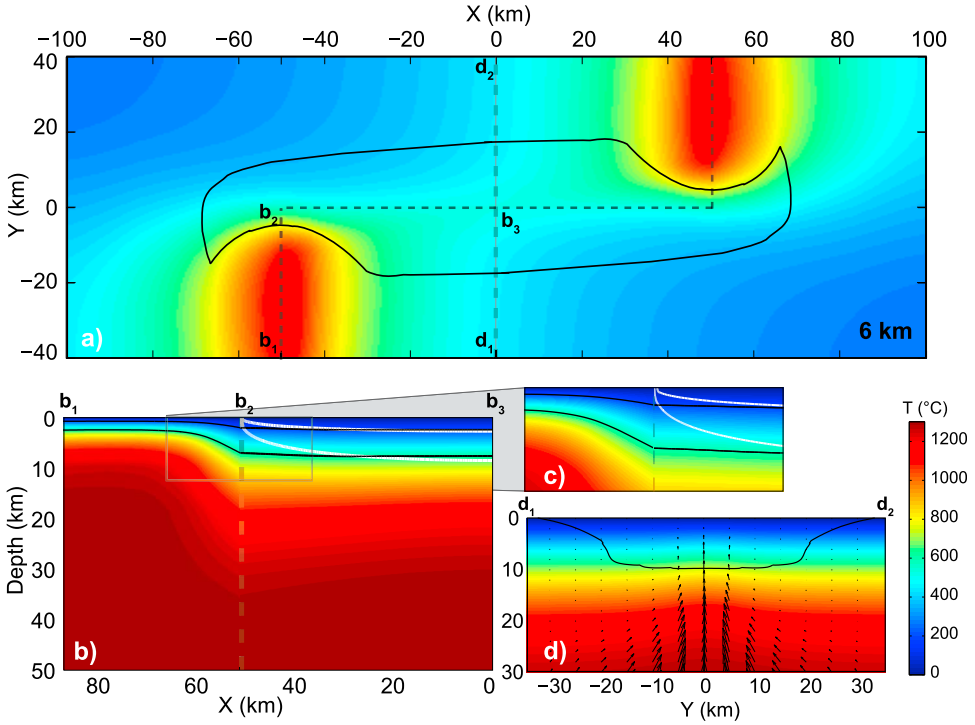

Figure 4. Base model solution with $u_0 = 3.0$ cm/yr and $L_T = 100$ km. Hydrothermal cooling, alteration, and shear heating feedbacks are not incorporated. (a) Map view of temperature at 6 km depth. Solid black line outlines zone of brittle deformation. Dashed lines and letter labels indicate the location of along-fault and across-fault profiles in Figures 4b and 4d, respectively. (b) Cross section along the ridge and transform fault. Solid black lines outline the calculated 350°C and 600°C isotherms. White lines show the location of the same isotherms calculated from a half-space cooling model. The half-space approximation is determined as an average of the temperatures calculated from each side of the fault using a lithospheric 2-D half-space cooling model that assumes conductive cooling with plate age [*McKenzie*, 1969]. (c) Expanded view of the of ridge-transform intersection, highlighting the shape of the isotherms from the numerical and half-space model calculations at the end of the transform fault. (d) Cross section perpendicular to the center of the fault. Solid black line indicates the maximum depth of brittle deformation. Arrows illustrate the velocity field and focused mantle upwelling in the center of the fault.

slip rates and fault lengths (Figures 5a and 6a). However, solutions calculated using the half-space model are characterized by a lithosphere that cools and thickens with distance from the ridge-transform intersection and isotherms that gradually deepen toward the center of the transform fault (white lines in Figures 4b and 4c). In contrast, isotherms predicted from our model deepen more steeply near the ridge, and then flatten, maintaining a relatively constant depth to center of the fault (Figures 4b and 4c). As a result, the width of the seismogenic zone is uniform along most of the fault (Figure 5b). Below, we discuss the effects of weakening due to mantle alteration, shear heating, and hydrothermal cooling on our thermal results.

3.1. Frictional Weakening

[26] The colder thermal structures predicted for longer faults and slower slip rates result in brittle deformation and zones of hydrous alteration that extend deeper into the lithosphere. However, frictional weakening associated with serpentinization results in negligible changes to the thermal structure. For example, models in which the friction coefficient is lowered within the zone of serpentinization, show changes in Z^m_{600} and A_{600} on the order of 0.1 km and 1%, respectively, for a fault with u_0 = 3.0, L_T = 100 km.

[27] We further explore the sensitivity of our results to fault weakening, using constant values of the friction parameters (μ, C) throughout the entire model space (Figure 7). μ and C limit the maximum differential stress in the brittle part of the lithosphere. Three trends are found between frictional strength and fault thermal structure, highlighted by arrows in Figure 7b. First, as C increases, the amount of passive mantle upwelling beneath the transform decreases, resulting in less heat transport to the fault

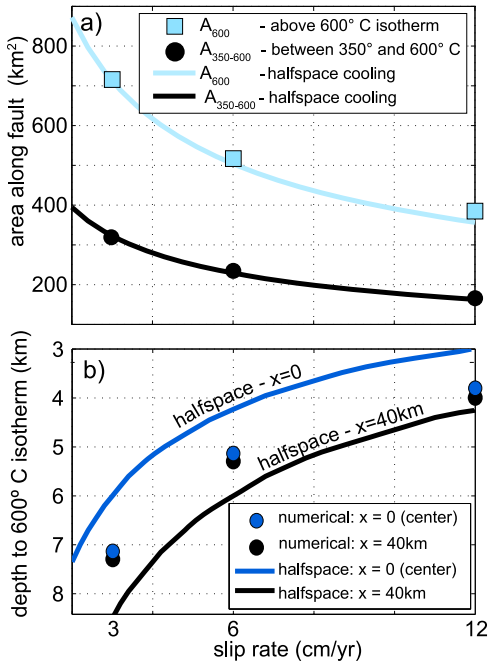

Figure 5. (a) A_{600} (light blue squares) and $A_{350–600}$ (black circles) as a function of slip rate for the base model assuming L_T = 100 km. Light blue and black lines indicate the same calculations made using a half-space cooling model. (b) Depth to the 600°C isotherm calculated at two locations along the fault. Black circles indicate the depth calculated at a distance 0.1 L_T away from the end of the fault (X = ±40 km for a 100 km fault). Blue circles indicate the depth at 0.5 L_T (X = 0, the center of the fault). Black and blue lines indicate the depth to the 600°C isotherm calculated using a half-space cooling model.

and cooler fault temperatures (trend I in Figure 7b). Second, for models with C = 10–40 MPa, decreasing μ leads to more localized strain along the fault. This also reduces advective heat transport into the fault domain, leading to cooler temperatures (trend II in Figure 7b). Finally, when the C <~ 3 MPa the lithosphere cannot support large differential stresses. In this case, decreasing μ promotes modest strain localization, which facilitates mantle upwelling along the transform and slightly warmer fault solutions (trend III in Figure 7b). Overall, for the range of μ and C examined, the total change in the calculated temperature structure is relatively small, ~1 km in Z^m_{600} over all frictional parameters.

3.2. Shear Heating

[28] Models that incorporate shear heating show a small increase in temperature along the fault (Figure 6). The magnitude of the temperature increase associated with shear heating scales with the fault length. For example, a transform of length L_T = 100 km produces a positive temperature anomaly of 20°C, while a transform of length, L_T = 500 km produces an anomaly of ~45°C. However, even for the longest transforms we examined, including shear heating only decreases A_{600} by ~1% and Z^m_{600} by <1 km relative to the base model (Figure 6). This results because Q_{sh} is largest along the base of the fault zone, where strain rate and effective confining stress are high. As shear heating warms the base of the fault, the brittle-ductile transition shallows, due to the temperature dependence of viscosity. This reduces Q_{sh} and effectively buffers the effect of shear heating on fault thermal structure.

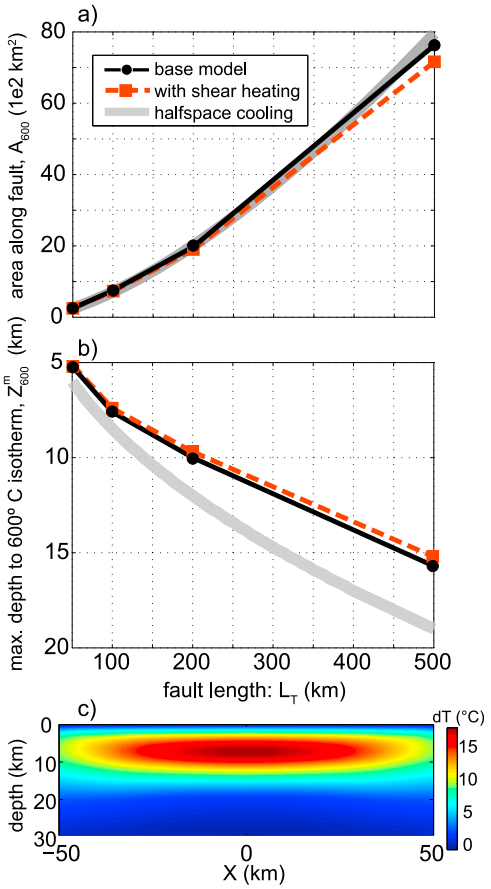

Figure 6. (a) A_{600} and (b) Z^m_{600} as a function of fault length (L_T) for the base model (black circles), the base model plus shear heating (red squares), and the half-space cooling model (solid grey line) with u_0 = 3.0 cm/yr. (c) Temperature difference between the base model solution and that with a shear heating heat source for u_0 = 3.0 cm/yr and L_T = 100 km.

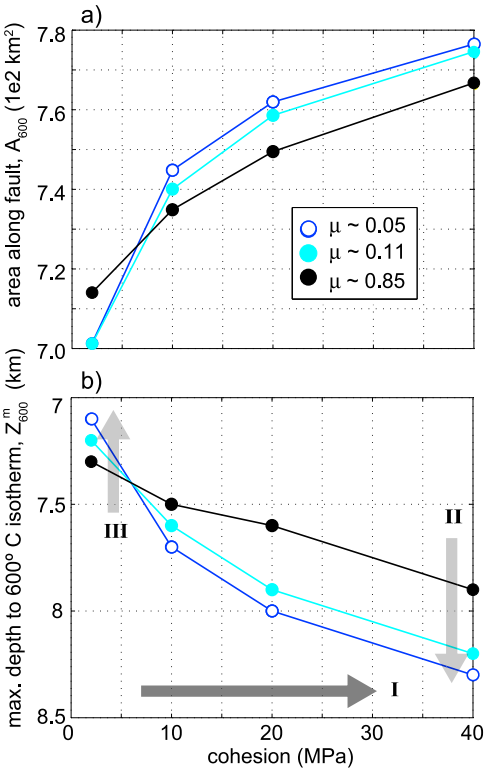

Figure 7. Summary of the change in (a) A_{600} and (b) Z^m_{600} as a function of cohesion (x axis) and friction coefficient (μ, black, cyan, and blue curves). Each symbol illustrates an individual model run. Arrows in Figure 7b indicate three trends in the dependence of temperature on lithospheric strength, which are outlined in section 3.1.

3.3. Hydrothermal Cooling

[29] For all transform geometries, hydrothermal cooling has a significant effect on the derived thermal structure. As the efficiency of fluid circulation increases (simulated by higher Nu), transform faults become progressively cooler. For models with Z_{ref} = 6 km, the most significant cooling occurs between Nu = 1–4 (Figure 8) with smaller changes for Nu > 4.

[30] The decrease in relative cooling for higher Nusselt numbers reflects the importance of the permeability structure for limiting hydrothermal circulation in regions of thick lithosphere. Initially, as Nu increases, the greater efficiency of hydrothermal circulation rapidly cools the transform. However, as the effective thermal conductivity continues to increase, heat flow becomes limited by the assumed pressure dependence of permeability. We explore this effect by varying Z_{ref}, the approximate depth of pore closure. For Z_{ref} = 6 km, Z^m_{600} increases by less than 2 km between Nu = 2 and Nu = 8, regardless of slip rate or fault length. In contrast, for Z_{ref} = 15 km, the region of high permeability extends to greater depths, and Z^m_{600} increases by ~5 km for the Nu = 8, slow slipping solution (Figure 8b).

4. Discussion

[31] Our numerical model provides insight into the size and shape of the seismogenic zone along oceanic transform faults. It also serves as a tool for estimating the amount of alteration along the transform and in the surrounding lithosphere. We find that both the size of the seismogenic zone and the extent of mantle hydration increase for longer faults, slower slip rates, and more efficient hydrothermal circulation. Below, we discuss the implications of our results for seismicity at oceanic transform faults

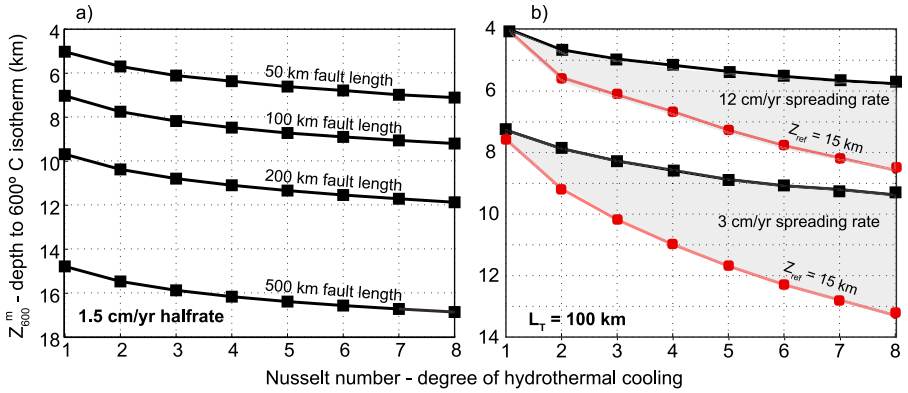

Figure 8. Z^m_{600} as a function of the efficiency of hydrothermal cooling (Nu) for different (a) slip rates and (b) fault lengths. Solutions associated with models with efficient hydrothermal cooling (high Nu), slower slip rates, and/or longer faults show Z^m_{600} extending into the upper oceanic mantle (z > 6 km). Black lines indicate model runs with Z_{ref} = 6 km. Red lines indicate model runs with Z_{ref} = 15 km. Each square represents results from an individual model solution.

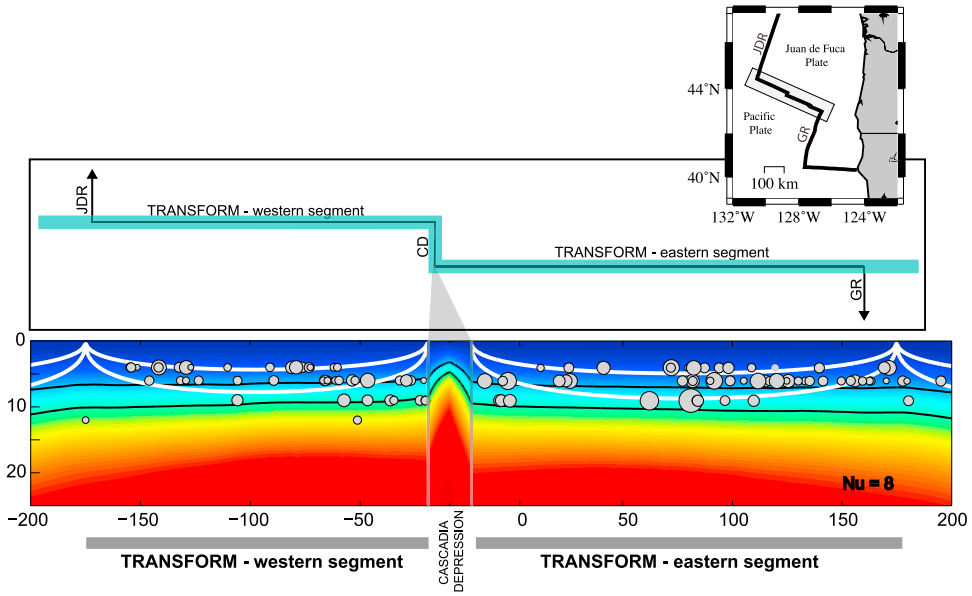

Figure 9. Temperature structure calculated for the Blanco Transform fault assuming u_0 = 5.6 cm/yr and Nu = 8. Two active fault segments are separated by the 20 km Cascadia Depression. The lengths of the western and eastern segments are 155 and 195 km, respectively. White lines indicate the 350°C and 600°C isotherms calculated from a half-space cooling mode. Black lines indicate the same isotherms for the numerical model. Grey circles show the centroid depth distribution of quality A (i.e., best fit location within 3 km of 5% variance increase bound) strike-slip events from *Braunmiller and Nábělek* [2008]. Size of circle is approximately proportional to the magnitude of the individual earthquake.

and their role in the transport of water from the hydrosphere to the upper mantle.

4.1. Implications for Oceanic Transform Fault Seismicity

[32] The seismogenic area estimated from either $A_{350–600}$ or A_{600} is remarkably consistent between our model results and those derived from the half-space model (Figures 5 and 6). This result implies that half-space models can be used to accurately estimate seismic coupling across oceanic transform faults. However, our models show significant differences in the geometry of the seismogenic zone compared to that predicted by the half-space cooling model. Specifically, the upper and lower isothermal bounds on the seismogenic zone deepen quickly near the ridge-transform intersection and then maintain a constant depth along the length of the fault. This differs from the seismogenic zone predicted from the half-space cooling model, in which isotherms deepen gradually with distance from the ridge-transform intersection to the center of the fault. The seismogenic width predicted from the half-space model thus thickens appreciably toward the center of the fault, in contrast to our numerical results that predict the seismogenic width remains nearly constant (Figure 4).

[33] To date, local and global-scale studies of oceanic transform fault seismicity have not definitively resolved any deepening of seismicity toward the center of transform faults. For example, ocean bottom seismic studies indicate the depth of seismicity along the Orozco [*Trehu and Solomon*, 1983] and Kane [*Wilcock et al.*, 1990] transform faults show no systematic deepening away from the ridge-transform intersection. Teleseismic body wave inversions [*Bergman and Solomon*, 1988; *Abercrombie and Ekstrom*, 2001] correlate earthquake distributions along the fault with the average depth of the 600°C isotherm predicted by the half-space model, but are unable to resolve along fault variations in focal depths.

[34] A regional inversion of surface waves from the Blanco transform also shows relatively constant fault width [*Braunmiller and Nábělek*, 2008]. In Figure 9 we compare earthquake depths along the Blanco transform with the thermal structures derived from half-space cooling and our model. In both models, we incorporate the Cascadia Depression as an intratransform spreading center, motivated by observations from seismic reflection data [*Embley et al.*, 1987], as well as the morphological expression of the offset [*Embley and Wilson*, 1992] and

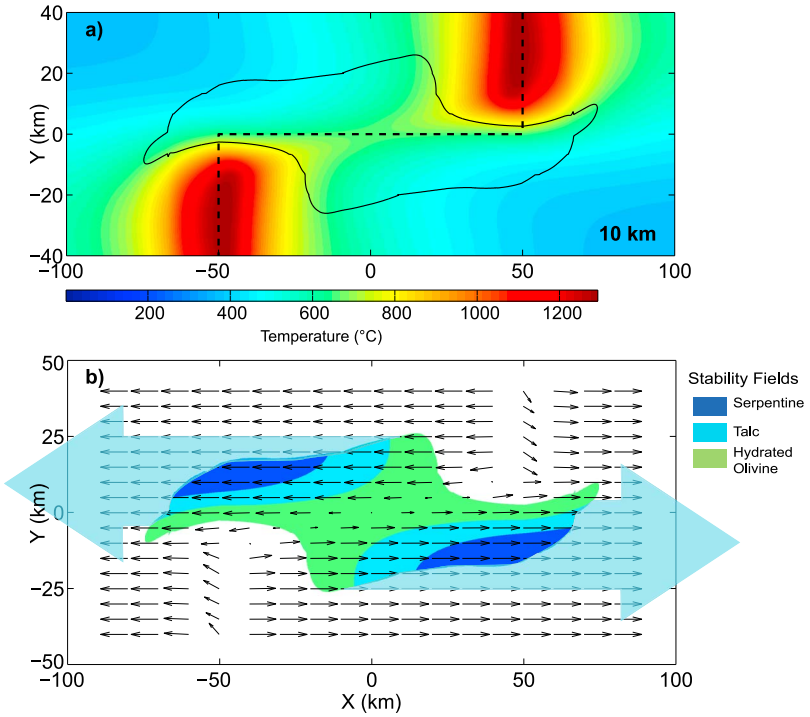

Figure 10. (a) Temperature solution at 10 km depth for a slow slipping transform fault (u_0 = 3.0 cm/yr) with efficient hydrothermal cooling, *Nu* =8. Black line outlines zone of brittle deformation where permeability may provide for fluids to reach mantle depths. (b) Estimated zones of stable hydrous phases at 10 km based on phase stability field of *Poli and Schmidt* [2002]. Light blue arrows indicate the advection of hydrated material, which is carried with plate motion off axis.

earthquake T axes [*Braunmiller and Nábělek*, 2008]. We find that while the half-space cooling model predicts the approximate maximum depth of seismicity at the center of the active eastern and western Blanco segments, it significantly underpredicts the depth of seismicity surrounding the ridge-transform intersections and the Cascadia Depression. In contrast, our numerical model predicts deeper seismicity near the end of the fault segments, in better agreement with the observed earthquake depths. Assuming hydrothermal circulation with *Nu* = 8 results in a good fit of the 600°C isotherm with the lower limit of seismicity along each of the fault segments. This Nusselt number is consistent with the preferred value used by *Phipps Morgan and Chen* [1993] to match magma lens depths along the global ridge system. The *Nu* = 8 model predicts that some of the Blanco earthquakes occur in lithosphere cooler than 350°C. The 350°C isotherm approximates the upper bound on the seismogenic zone based on the frictional characteristics of serpentine, which may not be present in the zones of shallow seismicity located within the crust. Thus, it appears that our model does a better job capturing the seismogenic zone of the Blanco transform as compared to the half-space cooling model.

4.2. Hydration of the Oceanic Mantle at Transform Faults

[35] Transform faults have long been recognized as tectonic settings where the mantle may undergo extensive alteration and serpentinization [*Bonatti and Honnorez*, 1976; *Francis*, 1981; *Dick*, 1989; *Cannat et al.*, 1995; *Detrick et al.*, 1987, 1993; *Canales et al.*, 2000]. Results from our numerical models provide a basis for quantitatively estimating the amount of hydration expected in transform settings. Simulations of relatively longer faults and slower slip rates show that brittle deformation extends into the upper mantle (Figure 4). Incorporating hydrothermal cooling further increases the depth of brittle deformation. In Figure 10 we show the calculated stability of antigorite and talc [*Poli and Schmidt*, 2002] at a depth of 10 km for a slow slipping transform fault. Figure 10 illustrates the enhanced hydration surrounding the transform fault

relative to the adjacent ridge axes, and shows how this region of alteration may be advected off axis.

[36] Hydrated peridotite is capable of transporting significant amounts of water to the arc melting region and postarc depths in subduction zones [*Hacker*, 2008]. Thus, the subduction of oceanic mantle that is hydrated at transform faults may promote arc magmagenesis and contribute appreciably to the flux of water to the deep mantle. Several studies have identified alteration at fracture zones as localized sources of water in the subducting slab. *Grove et al.* [2002] suggest that H_20-rich lavas erupted from Mount Shasta were derived from the dehydration of subducted serpentine that formed along the Blanco transform. Similarly, highly localized, water-rich magmas found along the Andean Southern Volcanic Zone have been correlated with the subduction of lithosphere influenced by the Mocha Fracture zone [*Rodríguez et al.*, 2007]. Future studies are required to determine whether there is a spreading rate dependence to the transport of water into the mantle, as would be predicted from our calculations.

5. Conclusions

[37] We have developed a new rheologic model to calculate the thermal structure of oceanic transform faults, which incorporates both nonlinear viscosity and brittle deformation into a viscoplastic rheology. We also incorporate the effects of three key feedbacks: frictional weakening due to mantle alteration, shear heating, and hydrothermal circulation.

[38] Numerical results predict cooler thermal structures for longer faults and slower slip rates. Although frictional weakening due to alteration may affect the mechanical properties of fault zones, we find that such weakening has a negligible effect on the resulting thermal structure. Similarly, incorporating shear heating leads to only slightly warmer thermal profiles. Hydrothermal circulation, conversely, has a significant cooling effect on the temperature structure in the transform zone, particularly in models with deep, efficient circulation.

[39] Our model can be used to estimate the geometry of the seismogenic zone and the degree of mantle hydration along oceanic transform faults. In contrast to the predictions made using the analytic half-space cooling model, our model predicts that the seismogenic zone along transform faults has a relatively uniform width, consistent with seismic observations. However, the total seismogenic area predicted from the two models is similar. For fault solutions with longer fault lengths and slow slip rates, we predict cooler temperature structure and brittle deformation that extends into the upper mantle. Alteration and subsequent subduction of such zones may play an important role in melting and arc volcanism at subduction zones. The results of our study are a first step toward developing a means of mapping the extent of serpentinization around transform faults that can be quantitatively correlated with along-arc geochemical anomalies.

Acknowledgments

[40] We would like to thank T. Grove, P. Fryer, J. McGuire, M. Boettcher, and T. Jordan for helpful discussions during the completion of this work. We would also like to thank T. Becker, C. Hieronymus, and R. Govers for their help improving this paper as well as R. Yanick for constructive comments on an earlier version of this manuscript. The material presented here is based on work supported by the National Science Foundation Division of Ocean Sciences (OCE) grants 0623188 (M.B. and G.H.) and 0649103 (M.B.) and Division of Earth Sciences (EAR) grant 0814513 (G.H.).

References

Abercrombie, R. E., and G. Ekstrom (2001), Earthquake slip on oceanic transform faults, *Nature*, *410*, 74–77, doi:10.1038/35065064.

Behn, M. D., J. Lin, and M. T. Zuber (2002), Mechanisms of normal fault development at mid-ocean ridges, *J. Geophys. Res.*, *107*(B4), 2083, doi:10.1029/2001JB000503.

Behn, M. D., M. S. Boettcher, and G. Hirth (2007), Thermal structure of oceanic transform faults, *Geology*, *35*, 307–310, doi:10.1130/G23112A.1.

Bergman, E. A., and S. C. Solomon (1988), Transform fault earthquakes in the North Atlantic: Source mechanisms and depth of faulting, *J. Geophys. Res.*, *93*(B8), 9027–9057.

Bird, P., Y. Y. Kagan, and D. D. Jackson (2002), Plate tectonics and earthquake potential of spreading ridges and oceanic transform faults, in *Plate Boundary Zones*, *Geodyn. Ser.*, vol. 30, pp. 203–218, AGU, Washington, D. C.

Boettcher, M. S., and T. H. Jordan (2004), Earthquake scaling relations for mid-ocean ridge transform faults, *J. Geophys. Res.*, *109*, B12302, doi:10.1029/2004JB003110.

Boettcher, M. S., G. Hirth, and B. Evans (2007), Olivine friction at the base of oceanic seismogenic zones, *J. Geophys. Res.*, *112*, B01205, doi:10.1029/2006JB004301.

Bonatti, E., and J. Honnorez (1976), Sections of the Earth's crust in the equatorial Atlantic, *J. Geophys. Res.*, *81*(23), 4140–4116.

Brace, W. F., and D. L. Kohlstedt (1980), Limits on lithospheric stress imposed by laboratory experiment, *Geophys. Res. Lett.*, *85*(B11), 6248–6252.

Braunmiller, J., and J. Nábělek (2008), Segmentation of the Blanco Transform Fault Zone from earthquake analysis: Complex tectonics of an oceanic transform fault, *J. Geophys. Res.*, *113*, B07108, doi:10.1029/2007JB005213.

Brun, J., and P. Cobbold (1980), Strain heating and thermal softening in continental shear zones: A review, *J. Struct. Geol.*, *2*, 149–158, doi:10.1016/0191-8141(80)90045-0.

Canales, J. P., J. L. R. S. Detrick, and J. A. Collins (2000), Crustal and upper mantle seismic structure beneath the rift mountains and across a nontransform offset at the Mid-Atlantic Ridge (35n), *J. Geophys. Res.*, *105*, 2699–2719.

Cannat, M., et al. (1995), Thin crust, ultramafic exposures, and rugged faulting patterns at the Mid-Atlantic Ridge (22°–24°N), *Geology*, *23*, 49–52, doi:10.1130/0091-7613(1995)0230049:TCUEAR2.3.CO;2.

Chen, Y., and W. J. Morgan (1990), A nonlinear rheology model for mid-ocean ridge axis topography, *J. Geophys. Res.*, *95*, 17,583–17,604.

Cherkaoui, A. S. M., W. S. D. Wilcock, R. A. Dunn, and D. R. Toomey (2003), A numerical model of hydrothermal cooling and crustal accretion at a fast spreading mid-ocean ridge, *Geochem. Geophys. Geosyst.*, *4*(9), 8616, doi:10.1029/2001GC000215.

David, C., T. F. Wong, W. Zhu, and J. Zhang (1994), Laboratory measurement of compaction-induced permeability change in porous rocks: Implications for the generation and maintenance of pore pressure excess in the crust, *Pure Appl. Geophys.*, *143*, 425–456.

Detrick, R. S., M. H. Cormier, R. A. Prince, D. W. Forsyth, and E. L. Ambos (1987), Seismic constraints on the crustal structure within the Vema fracture zone, *J. Geophys. Res.*, *87*(B13), 10,599–10,612.

Detrick, R. S., R. S. White, and G. M. Purdy (1993), Crustal structure of North Atlantic fracture zones, *Rev. Geophys.*, *31*(4), 439–458.

Dick, H. J. B. (1989), Abyssal peridotites, very slow spreading ridges and ocean ridge magmatism, *Geol. Soc. Spec. Publ.*, *42*, 71–105.

Embley, R. W., and D. S. Wilson (1992), Morphology of the Blanco transform fault zone-NE Pacific: Implications for its tectonic evolution, *Mar. Geophys. Res.*, *14*, 25–45.

Embley, R. W., L. D. Klum, G. Massoth, D. Abbott, and M. Holmes (1987), Morphology, structure and resonance potential of the Blanco Transform Fault Zone, in *Geology and Resource Potential for the Continental Margin of Western North America and Adjacent Ocean Basins—Beaufort Sea to Baja California*, *Earth Sci. Ser.*, vol. 6, edited by D. W. Scroll, A. Grantz, and J. G. Vetter, pp. 549–562, Circum-Pac. Res. Counc., Houston, Tex.

Engeln, J. F., D. A. Wiens, and S. Stein (1986), Mechanisms and depths of Atlantic transform earthquakes, *J. Geophys. Res.*, *91*, 548–577.

Escartin, J., G. Hirth, and B. Evans (2001), Strength of slightly serpentinized peridotites: Implications for the tectonics of oceanic lithosphere, *Geology*, *29*, 1023–1026.

Fleitout, L., and C. Froidevaux (1980), Thermal and mechanical evolution of shear zones, *J. Struct. Geol.*, *2*, 159–164, doi:10.1016/0191-8141(80)90046-2.

Francis, T. J. (1981), Serpentinization faults and their role in the tectonics of slow spreading ridges, *J. Geophys. Res.*, *86*(B12), 11,616–11,622.

Furlong, K. P., S. D. Sheaffer, and R. Malservisi (2001), Thermal-rheological controls on deformation within oceanic transforms, The Nature and Tectonic Significance of Fault Zone Weakening, *Geol. Soc. Spec. Publ.*, *186*, 65–83.

Grove, T. L., S. W. Parman, S. A. Bowring, R. C. Price, and M. B. Baker (2002), The role of an H_20-rich fluid component in the generation of primitive basaltic andesites and andesites from the Mt. Shasta region, N California, *Contrib. Mineral. Petrol.*, *142*, 375–396.

Grove, T. L., N. Chatterjee, S. W. Parman, and E. Médard (2006), The influence of H_2O on mantle wedge melting, Earth Planet. *Sci. Lett.*, *249*(1–2), 74–89, doi:10.1016/j.epsl.2006.06.043.

Hacker, B. R. (2008), H_2O subduction beyond arcs, *Geochem. Geophys. Geosyst.*, *9*, Q03001, doi:10.1029/2007GC001707.

Hirth, G., and D. Kohlstedt (2003), Rheology of the upper mantle and the mantle wedge: A view from the experimentalists, in *Inside the Subduction Factory*, *Geophys. Monogr. Ser.*, vol. 138, edited by J. Eiler, pp. 83–105, AGU, Washington, D. C.

Kelley, D. S., and K. M. Gillis (2002), Petrologic constraints upon hydrothermal circulation, paper presented at InterRidge Theoretical Institute: Thermal Structure of Ocean Crust and Dynamics of Hydrothermal Circulation, Pavia, Italy.

Kirby, S. H. (1983), Rheology of the lithosphere, *Rev. Geophys.*, *21*(6), 1458–1487.

McKenzie, D. P. (1969), Speculations on the consequences and causes of plate motions, *Geophys. J. R. Astron. Soc.*, *18*, 1–32.

Moore, D. E., D. A. Lockner, M. Shengli, R. Summers, and J. D. Byerlee (1997), Strengths of serpentinite gouges at elevated temperatures, *J. Geophys. Res.*, *102*(B7), 14,787–14,801.

O'Hanley, D. S. (1996), *Serpentinites: Recorders of Tectonic and Petrological History*, 296 pp., Oxford Univ. Press, New York.

Phipps Morgan, J., and Y. J. Chen (1993), The genesis of oceanic crust: Magma injection, hydrothermal circulation, and crustal flow, *J. Geophys. Res.*, *98*, 6283–6297.

Phipps Morgan, J., and D. W. Forsyth (1988), Three-dimensional flow and temperature perturbations due to a transform offset: Effects on oceanic crustal and upper mantle structure, *J. Geophys. Res.*, *93*, 2955–2966.

Phipps Morgan, J., and E. M. Parmentier (1984), Lithospheric stress near a ridge-transform intersection, *Geophys. Res. Lett.*, *11*(2), 113–116.

Phipps Morgan, J., E. M. Parmentier, and J. Lin (1987), Mechanisms for the origin of mid-ocean ridge axial topography: Implications for the thermal and mechanical structure of accreting plate boundaries, *J. Geophys. Res.*, *92*, 12,823–12,836.

Poli, S., and M. W. Schmidt (2002), Petrology of subducted slabs, *Annu. Rev. Earth Planet. Sci.*, *30*, 207–235.

Reinen, L. A., J. D. Weeks, and T. E. Tullis (1994), The frictional behavior of lizardite and antigorite serpentinites: Experiments, constitutive models, and implications for natural faults, *Pure Appl. Geophys.*, *143*, 318–358.

Rodríguez, C., D. Sellés, M. Dungan, C. Langmuir, and W. Leeman (2007), Adakitic dacites formed by intracrustal crystal fractionation of water-rich parent magmas at Nevado de Longaví volcano (36.2 s; Andean southern volcanic zone, central Chile), *J. Petrol.*, *48*(11), 2033–2061.

Shen, Y., and D. W. Forsyth (1992), The effects of temperature- and pressure-dependent viscosity on three-dimensional passive flow of the mantle beneath a ridge-transform system, *J. Geophys. Res.*, *97*, 19,717–19,728.

Sleep, N. H. (1975), Formation of oceanic crust: Some thermal constraints, *J. Geophys. Res.*, *80*(29), 4037–4042.

Trehu, A. M., and S. C. Solomon (1983), Earthquakes in the Orozco transform zone: Seismicity, source mechanisms, and tectonics, *J. Geophys. Res.*, *88*(B10), 8203–8225.

Van Avendonk, H. J. A., A. J. Harding, J. A. Orcutt, and J. S. McClain (1998), A two-dimensional tomographic study of

the Clipperton transform fault, *J. Geophys. Res.*, *103*(B8), 17,885–17,899.

van Keken, P. E., et al. (2008), A community benchmark for subduction zone modeling, *Phys. Earth Planet. Inter.*, *171* (1–4), 187–197, doi:10.1016/j.pepi.2008.04.015.

Wiens, D. A., and S. Stein (1983), Age dependence of oceanic intraplate seismicity and implications for lithospheric evolution, *J. Geophys. Res.*, *88*, 6455–6468.

Wilcock, W. S. D., G. M. Purdy, and S. C. Solomon (1990), Microearthquake evidence for extension across the Kane transform fault, *J. Geophys. Res.*, *95*(B10), 15,439–15,462.

Zoback, M. D., and J. Townend (2001), Implications of hydrostatic pore pressures and high crustal strength for the deformation of intraplate lithosphere, *Tectonophysics*, *336*, 19–30.